Self-similar solutions of shallow water equations with porosity

Vincent Guinot, Carole Delenne, Sandra Soares-Frazão

Self-similar solutions of shallow water equations with porosity

VINCENT GUINOT, Professor, HSM-Polytech Montpellier-/Inria LEMON, Univ. Montpellier, France
Email: vincent.guinot@umontpellier.fr
CAROLE DELENNE, Lecturer, HSM-Polytech Montpellier-/Inria LEMON, Univ. Montpellier, France
Email: carole.delenne@umontpellier.fr
SANDRA SOARES-FRAZAO, Professor, iMMC, Université Catholique de Louvain, Belgium
Email: sandra.soares-frazao@uclouvain.be (corresponding author)

This is the preprint of a paper accepted for publication in Journal of Hydraulic Research, DOI location https://doi.org/10.1080/00221686.2022.2106598

ABSTRACT

Simulated free surface transients in periodic urban layouts have been reported to be self-similar in the space-time domain when averaged on the scale of the building period. Such self-similarity is incompatible with the head loss model formulae used in most porosity-based shallow water models. Verifying it experimentally is thus of salient importance. New dam-break flow laboratory experiments are reported, where two different configurations of idealised periodic buildings layouts are explored. A space-time analysis of the experimental water level fields validates the self-similar character of the flow. Simulating the experiment using the two-dimensional shallow water model also yields self-similar period-averaged flow solutions. Then, the Single Porosity (SP), Integral Porosity (IP) and Dual Integral Porosity (DIP) models are applied. Although all three models behave in a similar fashion when the storage and connectivity porosities are close to each other, the DIP model is the one that upscales best the refined 2D solution.

Keywords: Urban floods, scale model, porosity model, flux, source term

1 Introduction

Shallow water models with porosity have arisen over the past two decades as an alternative to classical two-dimensional shallow water models for the modelling of flows over complex topography and in complex geometries (Bates, 2000; Defina, 2000). Urban flood modelling has become a typical application field of such models (Chen et al., 2012; Guinot and Soares-Frazão, 2006; Hervouët et al., 2000; Özgen et al., 2016b; Sanders et al., 2008; Schubert and Sanders, 2012; Soares-Frazão et al., 2008; Viero and Valipour, 2017). Many variations of porosity models have been presented in the literature. The Single Porosity (SP) model (Bates, 2000; Defina, 2000; Guinot and Soares-Frazão, 2006; Hervouët et al., 2000) uses a single porosity to describe the flow storage and connectivity properties of the urban medium. The Integral Porosity (IP) model (Sanders et al. 2008) uses a storage and a connectivity porosity to incorporate the effects of urban anisotropy in the governing equations (Kim et al., 2015). Anisotropic conservation laws may also be defined to account for anisotropy in SP models (Viero and Valipour, 2017; Viero 2019) via a tensor formulation (Ferrari and Viero, 2020) or through a binary porosity indicator (Varra et al., 2020). A depth-dependent version is presented

in Özgen et al. (2016a). The Multiple Porosity model (MP) uses a partition of the urban domain into several flow regions, with different degrees of connectivity and anisotropy (Guinot, 2012). The approach bears similarities with the multilayer BCR/CRF approach proposed in Chen et al. (2012). The Dual Integral Porosity (DIP) model (Guinot et al., 2017) has been proposed as a variation of the IP model, with improved flux and source term formulae. A model with three porosity parameters has been proposed recently (Bruwier et al., 2017). Higher-order numerical schemes are proposed to further increase the accuracy of the results especially in cases with topographies (Ferrari et al., 2020).

Two key issues arise in the derivation and application of porosity-based shallow water models. The first is the flux model, the second is the source term model. The flux model has a direct influence on the wave propagation properties of the flow solutions. Very different wave propagation speeds are obtained for the SP, IP and DIP models (Guinot et al., 2017). This suggests that experiments featuring wave propagation properties may be instrumental in discriminating the various porosity models. Many models have been proposed for the source term arising from building drag, from drag coefficient-based formulae (Sanders et al., 2008) to drag tensors (Guinot et al., 2017) and generalized tensor formulations (Velickovic et al., 2017). All these models take the form of Equations Of State (EOS) involving the flow variables (the water depth, the flow velocity or unit discharge vector) that can be validated against steady flow experiments (see Velickovic et al., 2017). However, benchmarking the various available formulations with refined, transient flow simulations (Guinot, 2017; Guinot et al., 2017) indicates that an additional momentum dissipation mechanism is at work in the presence of positive transients. This momentum dissipation mechanism makes the wave propagation speeds different depending on whether the flow is falling or rising (Guinot et al., 2017). This effect had been foreseen in Guinot (2012) to arise from a particular configuration of the MP model. It cannot be modelled by a momentum source term in the form of an EOS because it acts directly on the wave propagation speeds of the transients. In the presence of sharp transients propagating along the preferential directions of the urban layout, this momentum dissipation term exerts a significant influence on the simulated flow behaviour (Guinot, 2017). However, to date, no experimental evidence of such a mechanism has been provided. While successful applications of porosity models against experimental data sets have been presented in the literature (Kim et al., 2015; Özgen et al., 2016b), the number of building blocks involved is often too small to allow for a conclusive interpretation of the results.

The present paper serves three objectives. The first is to present a data set for dam-break scale model experiments in idealized urban layouts. This data set is to be used for model validation and/or benchmarking. The modelled urban layout counts up to 20 building periods in the longitudinal direction, which, to our best knowledge, is the largest number of block periods used in transient, scale model experiments. The second objective is to benchmark the SP, IP and DIP models against these experiments and to assess the validity of the abovementioned transient momentum dissipation mechanism. The third objective is to check whether refined 2D shallow water models are accurate enough to reproduce the dam-break experiments reported here and may therefore be used to produce reference solutions for the benchmarking of porosity models.

Section 2 presents the models used in the benchmarking phase and the theoretical implications of the source term formulation on solution properties. Section 3 presents the experimental setup and results. Section 4 is devoted to model benchmarking. Conclusions are given in Section 5.

2 Porosity models and solution self-similarity

2.1 Porosity models

The present subsection details the various formulations explored in the present work. Three different porosity models are considered: the Single Porosity (SP) model, the Integral Porosity (IP) model, and the Dual Integral Porosity (DIP) model. The analysis is restricted to one-dimensional flow configurations for the sake of consistency with the experiments reported hereafter. The governing equations for the three models can be written as

$$\partial_t \mathbf{u} + \left(\mathbf{I} - \mathbf{M}\right)\partial_x \mathbf{f}\left(\mathbf{u}\right) = \mathbf{s} \tag{1a}$$

$$\mathbf{u} = \left[\phi_\Omega h, \phi_\Omega hu\right]^T, \quad \mathbf{s} = \left[0, s_x\right]^T \tag{1b}$$

$$\mathbf{f} = \begin{cases} \phi_\Omega \left[hu, hu^2 + gh^2/2\right]^T & \text{(SP)} \\ \phi_\Gamma \left[hu, hu^2 + gh^2/2\right]^T & \text{(IP)} \\ \left[\phi_\Omega hu, \dfrac{\phi_\Omega^2}{\phi_\Gamma} hu^2 + \phi_\Gamma gh^2/2\right]^T & \text{(DIP)} \end{cases} \tag{1c}$$

$$s_x = g\phi_\Omega h\left(S_0 - S_f\right) - C_D h|u|u \tag{1d}$$

$$\mathbf{M} = \mu\begin{bmatrix} 0 & 0 \\ 0 & \mu \end{bmatrix}, \quad \mu = \begin{cases} 0 & \text{if} \quad \partial_t h \le 0 \\ 1 & \text{if} \quad \partial_t h > 0 \end{cases} \tag{1e}$$

where **u**, **f** and **s** are respectively the conserved variable, flux and source term vectors, **I** and **M** are respectively the identity and momentum dissipation matrices, C_D is the building drag coefficient per unit depth, g is the gravitational acceleration, h is the water depth, S_0 and S_f are respectively the bottom slope and bottom friction slope, u is the x-flow velocity, ϕ_Ω and ϕ_Γ are respectively the storage and connectivity porosities, and μ is a dimensionless coefficient between 0 and 1 accounting for momentum dissipation. The shallow water equations are obtained as a particular case of the SP, IP and DIP models by setting $\phi_\Omega = \phi_\Gamma = 1$ and $C_D = \mu = 0$ in equations (1a-c). The SP model is a particular case of both the IP and DIP models with $\phi_\Omega = \phi_\Gamma$. The main difference between the three models lies in how the connectivity porosity ϕ_Γ acts on the fluxes. Originally introduced by Sanders et al. (2008), the connectivity porosity is the fraction of the frontal area available for mass and momentum transfer. While it is not relevant to the SP model, ϕ_Γ exerts a salient influence on the wave propagation speeds of the IP and DIP models. From a physical point of view, it should be taken smaller than ϕ_Ω in the IP model, so as to account for the effects of building obstruction on the flow. Using $\phi_\Omega < \phi_\Gamma$ in the IP model is known to increase the propagation speed of the waves artificially. In the DIP model, the configuration $\phi_\Omega < \phi_\Gamma$ is not permissible because it yields complex-valued wave speeds (Guinot et al., 2017), with the consequence that hyperbolicity is lost and initial- and boundary-value problems become ill-posed.

Two types of source term models have been proposed so far for porosity models: turbulent head loss model proportional to the square or another power of the flow velocity (Guinot and Soares-Frazão, 2006; Özgen et al., 2015; Sanders et al., 2008; Velickovic et al., 2017), and transient momentum dissipation models, active only when transients involving positive waves arise (Guinot, 2012; Guinot et al., 2017). In one-dimensional flow configurations, as explored in the present work, turbulent head loss models can be written as in equation (1d). This type of model, however, has been shown to be insufficient to reproduce the behaviour of transients involving positive waves (Guinot et al., 2017; Guinot, 2017). For this reason, the transient

momentum dissipation model (1a, e) has been proposed in Guinot et al. (2017). This model was validated against systematic refined 2D simulations of urban dam-break problems in (Guinot, 2017). A salient feature of this model is that it leads to self-similar solutions when applied to the solution of Riemann problems, a feature that was identified in (Guinot, 2012) and confirmed in (Guinot, 2017). The next subsection is devoted to the analysis of self-similar solutions.

2.2 Source term and solution self-similarity

The objective of the present section is to derive the conditions under which the solutions of the one-dimensional dam-break problem are self-similar when computed using porosity models in the presence of source terms. A solution **u** of the governing equations (1a-e) is said to be self-similar in (x,t) if it verifies the following condition:

$$\mathbf{u}(x,t)=\mathbf{v}(x/t)\Leftrightarrow\mathbf{u}(kx,kt)=\mathbf{u}(x,t)\ \ \forall k \tag{2}$$

It is inferred from equation (2) that **u** is constant along any straight line originating from the origin (0, 0) in the (x,t) plane (Figure 1).

Consider first equation (1a) without the momentum dissipation matrix **M**

$$\partial_t\mathbf{u}+\partial_x\mathbf{f}(\mathbf{u})=\mathbf{s} \tag{3}$$

The exact expression for the flux function **f** (SP, IP or DIP in equation (1c)) needs not be known at this stage. For a periodic one-dimensional building layout, the flux **f** is a function of **u** alone because the porosities can be taken uniform, by setting the averaging domains equal to one spatial period. Solutions of the one-dimensional, initial value dam-break problem fulfil equation (3) with the following initial conditions:

$$\mathbf{u}(x,0)=\begin{cases}\mathbf{u}_L & \text{for} \quad x<0\\ \mathbf{u}_R & \text{for} \quad x>0\end{cases} \tag{4}$$

Solution self-similarity is investigated as in Lax (1957). Introducing the variable change $(X,T)=(kx,kt)$ where *k* is an arbitrary constant, using the chain rule, dividing by *k* leads to

$$\partial_T\mathbf{u}+\partial_X\mathbf{f}(\mathbf{u})=\frac{1}{k}\mathbf{s} \tag{5a}$$

$$\mathbf{u}(X,0)=\begin{cases}\mathbf{u}_L & \text{for} \quad X<0\\ \mathbf{u}_R & \text{for} \quad X>0\end{cases}=\mathbf{u}(x,0) \tag{5b}$$

In the case $\mathbf{s}=0$, equations (5a-b) are equivalent to equations (3, 4). Consequently, $\mathbf{u}(X,T)=\mathbf{u}(x,t)$ and the self-similarity property (2) is valid.

When the source term s is non-zero, the solutions of the IVP (5a-b) are not necessarily self-similar. If s obeys an equation of state, that is, $\mathbf{s}=\mathbf{s}(\mathbf{u})$, equation (5a) is not invariant with respect to the scaling factor *k*. In contrast, self-similarity is preserved if the source term takes the form proposed in Guinot et al. (2017):

$$\mathbf{s}=\mathbf{M}(\mathbf{u})\partial_x\mathbf{f}(\mathbf{u}) \tag{6}$$

where **M** is a matrix, the coefficients of which are functions of **u**. Self-similarity is proved by introducing again the variable change $(X,T)=(k\,x,k\,t)$ into Equation (6). The chain rule $\partial_x=\partial_x X\ \partial_X=k\,\partial_X$ yields the following property for s

$$\mathbf{s}=\mathbf{M}(\mathbf{u})k\partial_X\mathbf{f}(\mathbf{u})=k\,\mathbf{M}(\mathbf{u})\partial_X\mathbf{f}(\mathbf{u}) \tag{7}$$

Substituting equation (7) into (5a) gives

$$\partial_T \mathbf{u} + \partial_X \mathbf{f}\left(\mathbf{u}\right) = \mathbf{M}\left(\mathbf{u}\right)\partial_X \mathbf{f}\left(\mathbf{u}\right) = \mathbf{s} \tag{8}$$

Equation (8) is identical to Equation (3). The form (6) thus leaves equation (5a) invariant with respect to the scaling factor *k* and the self-similarity property (2) is verified. A transient source term in the form (6) is proposed in the DIP model (Guinot et al., 2017) to account for the dissipation of momentum originating from positive transients propagating into building block layouts. Comparisons of DIP model outputs to pore-scale averaged refined shallow water simulations show that this source term is active only for rising water levels and that only this form of source term allows the wave propagation properties of transients to be preserved and accurate solutions to be reproduced (Guinot et al., 2017). Note that this source term alone is not sufficient to account for all energy losses because it is zero under steady state conditions, while significant steady state head losses have been reported when the flow is not aligned with the main street directions (Velickovic et al., 2017). However, it is predominant in the case of sharp transients propagating along the main street directions.

The self-similar behaviour of the solutions of the Riemann problem, if verified in reality, may serve as a powerful tool for discriminating between alternative momentum source term closures in shallow water models with porosity.

3 Experiments

3.1 Experimental set-up

Dam-break flow experiments were conducted at the Hydraulics Laboratory of the Institute of Mechanics, Materials and Civil Engineering (Université catholique de Louvain, Belgium). The flume is 29.5 m long and 1 m wide. The bed is horizontal and its Manning friction coefficient is estimated to be $n = 0.011$ s m$^{-1/3}$ from previous experiments (e.g. Soares-Frazão and Zech 2008, Velickovic et al., 2017). Two periodic block configurations were studied. In Configuration 1 (Figure 2), the blocks are placed in such a way that 3/4 of the flume section is obstructed and each block occupies a fraction 6/16 of the plan view area, therefore 62.5 % of the plan view area is available to water storage, and 25 % of the model width is available to the flow. This yields $\left(\varphi_\Omega, \varphi_\Gamma\right) = \left(0.625, 0.25\right)$. In Configuration 2 (Figure 3), the blocks occupy 30% of the total plan view area, thus making 70 % of the total area available for water storage, and half of the cross-section is periodically obstructed by the blocks. Consequently, $\left(\varphi_\Omega, \varphi_\Gamma\right) = \left(0.7, 0.5\right)$. The blocks are made of marine plywood presenting a very smooth surface, so that no additional friction effects are expected. The water was initially at rest in the upstream part of the flume, with an initial depth $h_0 = 0.350$ m. In the downstream part, a thin layer of water was present, with a depth ranging from 5 mm to 1.5 cm depending on the replicate. Since several experimental replicates were performed, the downstream depth, stemming from the residual water from the previous replicates, was not exactly the same for all replicates. The upstream and downstream sections of the flume were separated by a gate located 9.73 m from the upstream end of the flume. The gate was lifted very quickly (within less than 0.5 s) to simulate the breaking of a dam. The water level at each gauging point was measured using ultrasonic probes (Baumer) placed at a fixed distance above the flume. These probes record the distance to the water surface with an accuracy of 0.1 mm and a maximum temporal resolution of 0.05 s, depending on the number of simultaneous measurements. In addition to the probes located in the flume, a probe was placed in front of the gate in order to identify the starting time of the experiment ($t = 0$), thus allowing the signals collected from the other probes to be synchronized.

The water levels were recorded every 0.2 s using four probes, at 114 and 97 gauging points for Configurations 1 and 2 respectively, resulting in more than 300 experimental runs. The time span involved in these plots is [0 s, 30 s], with one block-averaged value every second. The gauging points are located along the main flow path and inside the cavities between two successive blocks (see Figure 2 for Configuration 1, Figure 3 for Configuration 2). The probes are labelled in the following way: PU*x_y* for a probe located in the upstream part at the coordinates $(-x, y)$ and PD*x_y* for a probe located in the downstream part at the coordinates (x, y). For example, probe PD1_125 is located in the downstream part, at $(x, y) = (1, 0.125)$ where the coordinates are expressed in m. Sample locations of the probes are given in Table 1 for Configuration 1 and Table 2 for Configuration 2.

The repeatability of the experiments was checked, so that measurements obtained from different runs could be combined. Indeed, more than 300 experimental runs in total were needed to cover the whole measurement range, so it is mandatory to check for the repeatability of the experiments in order to combine the results of the different runs into a single data set. The repeatability at probe PD2_125 is illustrated in Figure 4 for three different runs.

3.2 Results

The purpose is to check the self-similar character of the large-scale water depth field. To do so, it is necessary to devise a procedure to compute the block-averaged, experimental water depth fields. The block-averaged water depths are computed using all the experiment replicates:

$$h_{\mathrm{av}}(x_i, t) = \frac{1}{R}\sum_{j=1}^{R}\sum_{k=1}^{N} w_k h_{i,k,j}(x,t), \quad \sum_{k=1}^{N} w_k = 1 \qquad (9)$$

where $h_{i,k,j}$ is the water depth measured by the *k*th probe in the *i*th block period during the *j*th replicate, *N* and *R* are respectively the number of probes per block period and the number of experiment replicates, and w_k is the weight of the *k*th probe within a given block period. The averaging domain is centred around the lateral street, as shown in Figure 5. Figure 5 also shows the numbering scheme for the probes in Configuration 1. The sensitivity of the averaging results to the distribution of the weights w_k is assessed by using two strongly contrasted weight distributions, labelled A and B. The weight distributions for these two weighting approaches are given in Table 3. Approach A gives equal weight to all probes, while Approach B gives a 50% weight to the average of the probes within the lateral street, and 1/4 to each of the probes at the boundary of the averaging domain. Figure 6 shows the behaviour of h_{av} obtained for the two weighting approaches. The two curves are very close to each other, with differences much smaller than the measurement precision of the probes. Since no significant difference is observed between the two approaches, the equal weight approach is retained for Configuration 2.

The block-averaged water depth is plotted as a function of x/t for all block periods in Figure 7. Note that the time interval used for these plots is [0 s, 11 s] for Configuration 1 and [0 s, 9 s] for Configuration 2. This is because after these times, the dambreak waves are observed to reach the downstream or upstream end of the flume. The flow pattern at later times switches from an initial value problem to a boundary value problem and studying solution self-similarity becomes meaningless. Although the plots in Figure 7 seem to indicate that the experimental profiles gather along a single S-shaped curve in the $(x/t, h_{\mathrm{av}})$ plane, a certain amount of scattering is observed in the experimental data. In the case of a perfectly

self-similar solution, all experimental points should fall exactly onto a single curve. The question then arises whether the present scattering can be explained by experimental uncertainty.

This question is answered by incorporating the error boxes in the experimental plots. This is done in Figure 8 for Configuration 1 and Figure 9 for Configuration 2. The reader is referred to the electronic version of the paper, where the various series are plotted using different colours to allow for a better identification of the series. The experimental uncertainty for probe positioning was $\Delta x = \pm 1\,\text{cm}$.

The time resolution of the data logger is less than 1 s. But the uncertainty stemming from the estimation of the starting time ($t = 0$), identified using the probe placed in front of the gate, is estimated as +-2 s.

The uncertainty $\Delta h = \pm 1\,\text{cm}$ in the water depth is inferred from the min-max difference between the individual time series recorded by the probes. Let $h_{av}(x, t, j)$ be the average water depth obtained at location x_i at time t for the jth replicate. The uncertainty in the water depth is obtained by taking the difference between the maximum and minimum water depths obtained from the various replicates at the same time and location

$$\Delta h = \max_{x_i,t}\left(\max_j\left(h_{av}\left(x_i,t,j\right)\right) - \min_j\left(h_{av}\left(x_i,t,j\right)\right)\right) \tag{10}$$

This uncertainty is significantly larger than the measurement precision of the probes. It only illustrates the impossibility of obtaining perfectly replicable experiments. This is due to many factors. To start with, small time difference in the water depth time series from one replicate to the other may result in large depth differences because sharp fronts are dealt with. Moreover, oscillations with an amplitude up to 1.5 cm were observed in the upstream part of the experimental device during the filling phase, which makes it very difficult to guarantee that the upstream water level was exactly the same for all replicates. Lastly, a small leakage was observed across the gate during the filling phase before the replicates. Consequently, the downstream part of the channel was never completely dry between successive replicates. Also note that a number of outliers had to be removed from the experimental data set (in some occasions, initially dry beds were recorded by the probes as having an initial depth of -1.5 cm). As shown in Figure 8, for Configuration 1 it is possible to draw a curve intersecting all the experimental error boxes, except for a few block periods. The curve is a spline that is fitted by minimizing the following objective function.

$$J = \sum_{i,j,k} e_{i,j,k} \tag{11a}$$

$$e_{i,j,k} = \max\left(0, h_{i,j,k} - \frac{\Delta h}{2} - h_{\text{fit}}\left(x_i,t\right), h_{\text{fit}}\left(x_i,t\right) - h_{i,j,k} - \frac{\Delta h}{2}\right) \tag{11b}$$

Where $h_{\text{fit}}(x_i, t)$ is the fitted function. The fitting error $e_{i,j,k}$ is zero if the fitted h lies within the experimental error box, indicating that the difference between the fitted value and the experimental one can be explained by the experimental imprecision. If the fitted function value $h_{\text{fit}}(x_i, t)$ lies outside the experimental error box, it means that the experimental imprecision cannot explain fully the difference between the experimental values and the fitted ones. In this case, the error is taken as the distance between the fitted value and the nearest bound of the experimental error box. This approach was used in the past to maximize the plausibility of a model, that is, to determine a unique model setup that best explains the measurements in the light of the experimental error (see Majdalani et al. (2018) for detailed considerations on the approach). The series for $x = -1\,\text{m}$ and $x = 4\,\text{m}$ are clearly outliers. For Configuration 2 (Figure 9), the error boxes for the series $x = -2.50\,\text{m}$, $x = 1.25\,\text{m}$ and $x = 2\,\text{m}$ are not intersected by the fitted curve either. These few series excepted, the fitted curves are intercepted by the error boxes of all experimental series, which tends to validate the self-similar behaviour.

That the measurements at a given location depart from the expected self-similar behaviour may be explained by several factors. A first possible reason is the local invalidity of the hydrostatic pressure distribution assumption. The self-similar character of the solution is a direct consequence of the hyperbolic nature of the shallow water model. In the case of non-negligible vertical accelerations, the shallow water model becomes invalid and corrective terms, usually dispersive, must be incorporated in the governing equations. The solution of the Riemann problem for second- and higher-order partial differential equations is not self-similar in (x,t). This may explain for instance the behaviour of the experimental points $x=-1\,\mathrm{m}$ in Configuration 1 (Figure 8), because the first block period is located very close to the gate, in a region where the free surface is steep and vertical accelerations are not negligible. A second possible reason is a systematic error during probe recording and/or calibration. A third reason could be a consistent bias introduced by a slightly altered geometry. It is striking indeed to notice that, for a given block period, the records are consistently above or below the fitted curve. This seems to indicate a consistent behaviour of the hydrodynamics of the block period under consideration. That a given block average departs significantly from the rest of the series might be due to an altered geometry compared to the ideal layout (e.g. a block slightly shifted or with dimensions slightly different compared to specifications, etc.). The outlying series in Figures 8 and 9 can be attributed to a combination of all these reasons.

4 Model results and discussion

4.1 Results

The experiments are simulated using four models: the two-dimensional shallow water model, the Single Porosity (SP) model, the Integral Porosity (IP) model, and the Dual Integral Porosity (DIP) model. The 2D shallow water model uses a 1 cm×1 cm square grid, which results in more than 140,000 elements. The 2D shallow water equations are solved using the finite volume-based, MUSCL-EVR technique (Soares-Frazão and Guinot, 2007), with a maximum CFL of unity (see Soares-Frazão and Guinot, (2007) for the derivation of the stability criterion). The porosity models are one-dimensional. The governing equations for the three porosity models are not solved numerically but semi-analytically. The first generalized Riemann invariant (Lax, 1957) is integrated across the rarefaction wave that connects the left state to the intermediate region of constant state:

$$\mathrm{d}\mathbf{u}//\mathbf{K}^{(1)} \quad \text{across} \quad \frac{\mathrm{d}x}{\mathrm{d}t}=\lambda_1 \tag{12}$$

Where $\mathbf{K}^{(1)}$ and λ_1 are respectively the first eigenvector and eigenvalue of the Jacobian matrix of **f** with respect to **u**. Owing to the simple structure of the Jacobian matrix, the matrix of eigenvectors in shallow water models is given by

$$\mathbf{K}=\begin{bmatrix}1 & 1\\ \lambda_1 & \lambda_2\end{bmatrix} \tag{13}$$

Consequently, the first generalized Riemann invariant across the *p*th wave is given by

$$\mathrm{d}u_2=\lambda_1\mathrm{d}u_1 \quad \text{across} \quad \frac{\mathrm{d}x}{\mathrm{d}t}=\lambda_1 \tag{14}$$

where $u_k\ (k=1,2)$ is the *k*th component of **u**. The formulae for the wave propagation speeds in the SP, IP and DIP models are given in (Guinot et al., 2017). While Equation (14) can be integrated analytically for the SP and IP models, its integration for the DIP model is performed using an RK2 procedure with a depth increment $\delta h=1\,\mathrm{cm}$.

All simulations are run using the initial condition (h_L, h_R) = (0.35 m, 0 m). The fine grid solution computed every 0.1 second by the two-dimensional shallow water model is averaged over the block periods in order to allow for a comparison with the experimental results.

The results of the refined 2D shallow water model are compared to the experimental results in Figure 10. It is noticed that the refined 2D solution also tends to follow an S-shaped curve. Only do a few points strongly depart from the main trend. Inspecting the period-averaged results shows that these points belong to the block periods in the immediate neighbourhood to the initial discontinuity. This tends to confirm the finding by Guinot (2017) that more than one spatial period may be needed to observe the self-similarity of the refined solution. While the block-averaged refined 2D solution quite closely follows the experimental data in Configuration 1 (Figure 10, top), it fails to replicate the curvature and the sudden steepening of the data cloud near $x/t = 0$ in Configuration 2 (Figure 10, bottom).

The results of the SP, IP and DIP models are plotted together with the experimental data in Figure 11. For Configuration 1, the combination of porosities $(\phi_\Gamma, \phi_\Omega) = (0.25, 0.625)$ yields strongly contrasted model responses. The SP model consistently overestimates the propagation speed of the transient. The IP model fails to reproduce the change in the curvature of the free surface in the upstream part of the flume (negative x/t values) but reconstructs successfully the downstream part. This, however, is regarded as a mere coincidence in that the refined 2D model (of which the porosity model is supposed to be an approximation) is not as good as the IP model in this part of the profile. Of the three porosity models, the DIP model is the only one that combines a successful reproduction of the curvature in the upstream part of the flume with a satisfactory approximation of the experimental behaviour in the downstream part. For Configuration 2, the contrast between the two porosities $(\phi_\Gamma, \phi_\Omega) = (0.5, 0.7)$ is much milder and all three models behave in a very similar fashion. All three fail to reproduce the steepening of the profile near $x/t = 0$, just as the refined 2D model does. Nevertheless, the DIP model is the most successful of the three in upscaling the refined 2D shallow water solution in both configurations.

4.2 Discussion

Besides setting up an experimental database, an objective of the present work was to check the relevance of incorporating a transient momentum dissipation term in the governing equations of porosity models. The three model outputs plotted in Figure 11 seems to indicate that such a momentum dissipation model is of limited interest, at least for the flow configurations reported here. The reason is that the transient momentum dissipation model operates only when the free surface is rising (thus only for positive x/t) and its main effect is to slow down the propagation of the waves. In Configuration 1, it may allow the downstream part of the SP profile to be corrected to fit better the experimental results, but it would have no action on the upstream part of the profile. Correcting the propagation speeds of the IP and DIP profiles for $x/t > 0$ would only contribute to increase the discrepancy between these profiles and the experimental points, so introducing dissipation in these two models is not advisable. In configuration 2, all three models exhibit similar behaviours and fit the experimental data rather well in the region $x/t > 0$. Consequently, slowing down the propagation speeds in this region is of limited interest. The main discrepancy with the experimental results of Configuration 2 is observed in the upstream part of the flume, a region over which the free surface is falling, thus cancelling the transient momentum dissipation term.

A salient feature of the modelling is that all models, including the refined 2D shallow water model, fail to reproduce the steep part of the experimental profiles near $x/t = 0$. This may be attributed to strong vertical accelerations occurring at the gate at the early times of the experiment. Such acceleration may modify locally the pressure field compared to the theoretically hydrostatic pressure distribution. This may result in modified wave propagation speeds and altered free surface profiles compared to those given by the solution of the shallow water equations.

As shown in Figures 10 and 11, the water depth profile is much better reproduced by all models for Configuration 1 than for Configuration 2. This can be explained by a number of factors. First, the water depth profile is much steeper near $x/t = 0$ in Configuration 2 than in Configuration 1. Consequently, vertical accelerations are much stronger in Configuration 2 than in Configuration 1, thus making the hydrostatic pressure distribution assumption more questionable in the second configuration than in the first, especially in the neighbourhood of the gate. Second, the ratio ϕ_Γ/ϕ_Ω is larger in Configuration 2 than in Configuration 1. Therefore, the positive and negative waves propagate faster along the main channel in the second configuration. This entails stronger reflection phenomena against the walls of the building blocks and within the lateral streets, with the consequence that difference between the water depths and velocities in the main street and in the lateral ones is larger in Configuration 2. Almost all porosity models (except for the MP model) being based on the assumption of a uniform distribution of the water levels and the flow velocity within an averaging block, the more transient the configuration, the more inaccurate this underlying assumption.

5 Conclusions

An experimental data set for laboratory scale dam-break experiments in idealized urban layouts is presented. The experiments are carried out using a scale model of periodic, aligned building blocks. Two geometric configurations, corresponding to two different storage and connectivity porosity combinations, are used: $(\phi_\Omega, \phi_\Gamma) = (0.625, 0.25)$ and $(\phi_\Omega, \phi_\Gamma) = (0.7, 0.5)$. The water levels are recorded as functions of time at 6 points in each block period. The experimental, block-averaged values are shown to obey a self-similar behaviour in the (x,t) space.

The experiment is reproduced satisfactorily using a two-dimensional refined shallow water model, except in the close neighbourhood of the initial discontinuity. The block-averaged water depths computed by the refined 2D model are also shown to follow a self-similar behaviour. A theoretical analysis shows that the self-similar behaviour can be preserved by a pore scale-averaged model only if the momentum source term does not obey an equation of state but is a function of the momentum flux divergence. This is the case of the transient momentum dissipation term introduced in the DIP model. Reproducing the experiments using the SP, IP and DIP models shows that (i) the DIP fluxes outperform the SP and IP fluxes when the contrast between the connectivity and storage porosities is large ($\phi_\Omega / \phi_\Gamma = 2.5$), (ii) all three models exhibit very similar behaviours for a ratio $\phi_\Omega / \phi_\Gamma = 1.4$, (iii) all models, including the refined 2D shallow water model, fail in reproducing the steep part of the water depth profiles near $x/t = 0$.

Lastly, while satisfactory in theory because it preserves solution self-similarity, the transient momentum dissipation term proposed in the DIP model (Guinot et al., 2017) is found useless to reproduce the present experiments. Many reasons may be given for this, such too small a number of block periods to allow for an accurate upscaling. Further research

should be directed to enriching the experimental database by exploring a wider range of flow conditions and geometries.

Acknowledgements

The authors wish to acknowledge the contribution of Fabiola Gangi, Gennaro Pileggi and Samuel Laurent in performing the laboratory experiments.

Funding

The financial support of Inria-LEMON in the form of researcher mobility funding is gratefully acknowledged.

Supplemental data

The detailed experimental data can be obtained upon request to the corresponding author.

Notation

CD = drag coefficient per unit depth (m^{-1})
f = flux vector
h = water depth (m)
k = scaling factor (-)
M = dissipation matrix
s = source term vector
S_0 = bottom slope
S_f = friction slope
T, t = time coordinates (s)
u = conserved variable vector
u, v = x- and y-flow velocities ($m\ s^{-1}$)
X, x = longitudinal space coordinates (m)
y = transverse space coordinate (m)
μ = momentum dissipation coefficient (–)

References

Bates, P.D. (2000). Development and testing of a subgrid-scale model for moving-boundary hydrodynamic problems in shallow water. Hydrological Processes, 14, 2073-2088.

Bruwier, M., Archambeau, P., Erpicum, S., Pirotton, M., Dewals, B. (2017). Shallow-water models with anisotropic porosity and merging for flood modelling on Cartesian grids. Journal of Hydrology, 554, 693-709.

Chen, A., Evans, B., Djordjevic, S., Savic, D.A. (2012). Multi-layer coarse-grid modelling in 2D urban flood simulations. Journal of Hydrology, 470, 1-11.

Defina, A. (2000). Two-dimensional shallow flow equations for partially dry areas. Water Resources Research, 36, 3251–64.

Ferrari, A.; Viero, D.P. Floodwater pathways in urban areas: A method to compute porosity fields for anisotropic subgrid models in differential form. J. Hydrol. 2020, 589.

Ferrari, A. Vacondio, R., Mignosa, P. 2020. A second-order numerical scheme for the porous shallow water equations based on a DOT ADER augmented Riemann solver. Advances in Water Resources, 140, 103587.

Guinot, V. (2012). Multiple porosity shallow water models for macroscopic modelling of urban floods. Advances in Water Resources, 37, 40-72.

480 Guinot, V. (2017). A critical assessment of flux and source term closures in shallow water
481 models with porosity for urban flood simulations. Advances in Water Resources,
482 109,133-157.
483 Guinot, V., Sanders, B.F., Schubert, J.E. (2017). Dual integral porosity shallow water model
484 for urban flood modelling. Advances in Water Resources, 103, 16-31.
485 Guinot, V., Soares-Frazão, S. (2006). Flux and source term discretisation in two–dimensional
486 shallow water models with porosity on unstructured grids. International Journal for
487 Numerical Methods in Fluids, 50, 309–345.
488 Hervouët, J.M. , Samie, R. , Moreau, B. (2000). Modelling urban areas in dam-break
489 floodwave numerical simulations. In: Proceedings of the international seminar and
490 workshop on rescue actions based on dambreak flow analysis, pp. 1–6 . Seinâjoki,
491 Finland.
492 Kim, B., Sanders, B.F., Falmigetti, J., Guinot, V. (2015). Urban flood modelling with porous
493 shallow water equations: a case study of model errors in the presence of anisotropic
494 porosity. Journal of Hydrology, 523, 680-692, 2015.
495 Lax, P.D. (1957). Hyperbolic systems of conservation laws II. Communications on Pure and
496 Applied Mathematics, 10, 537-566.
497 Majdalani, S., Guinot, V., Delenne, C., Gebran, H. (2018). Modelling solute dispersion in
498 periodic heterogeneous porous media: Model benchmarking against intermediate scale
499 experiments. Journal of Hydrology, 561, 427–443.
500 Özgen, I., Liang, D., Hinkelmann, R. (2016a) Shallow water equations with depth-dependent
501 anisotropic porosity for subgrid-scale topography. Applied Mathematical Modelling, 40,
502 7447-7473.
503 Özgen, I., Teuber, K., Smon, F., Liang, D., Hinkelmann, R. (2015). Upscaling the shallow
504 water model with a novel roughness formulation. Environmental Earth Sciences, 74,
505 7371-7386.
506 Özgen, I., Zhao, J., Liang, D., Hinkelmann, R.. (2016b). Urban flood modeling using shallow
507 water equations with depth-dependent anisotropic porosity. Journal of Hydrology, 54,
508 1165–1184.
509 Sanders, B.F., Schubert, J.E., Gallegos, H.A. (2008). Integral formulation of shallow water
510 equations with anisotropic porosity for urban flood modelling. J. Hydrol. 362, 19–38.
511 Schubert, J.E., Sanders, B.F. (2012). Building treatments for urban flood inundation models
512 and implications for predictive skill and modeling efficiency. Adv. Water Resour.
513 41,49–64.
514 Soares-Frazão, S., Guinot, V. (2007). An eigenvector-based linear reconstruction scheme for
515 the shallow water equations on two-dimensional unstructured meshes. International
516 Journal for Numerical Methods in Fluids, 53, 23–55.
517 Soares Frazão S., Zech Y. (2008). Dam-break flow through an idealised city. Journal of
518 Hydraulic Research, 46(5), 636-647.
519 Soares-Frazão, S., Lhomme, J., Guinot, V., Zech, Y. (2008). Two–dimensional shallow water
520 models with porosity for urban flood modelling. J. Hydraul. Res. 46, 45–64.
521 Varra G., Pepe V. Cimorelli L., Della Morte R., Cozzolino L. 2020. On integral and
522 differential porosity models for urban flooding simulation. Adv. Water Resour. 136,
523 103455
524 Velickovic, M., Soares-Frazão, S., Zech, Y. 2017. Steady-flow experiments in urban areas
525 and anisotropic porosity model. Journal of Hydraulic Research, 55, 85-100.
526 Viero D.P., Valipour M. 2017. Modeling anisotropy in free-surface over- land and shallow
527 inundation flows. Adv. Water Resour. 104, 1–14
528 Viero D.P. 2019. Modelling urban floods using a finite element staggered scheme with an
529 anisotropic dual porosity model. Journal of Hydrology, 568, 247-259
530

Table 1. Sample probe coordinates for Configuration 1. x-period: 1 m.

Identification	x (m)	y (m)
PU85_125	-8.500	0.125
PU8_125	-8.000	0.125
PU8_300	-8.000	0.300
PU8_455	-8.000	0.455
PU8_600	-8.000	0.600
PU8_800	-8.000	0.800

Table 2. Sample probe coordinates for Configuration 2. x-period: 1.25 m.

Identification	x (m)	y (m)
PU875_125	-8.750	0.150
PU875_375	-8.750	0.375
PU875_575	-8.750	0.575
PU875_800	-8.750	0.800
PU85_250	-8.500	0.250
PU8125_250	-8.125	0.250
PU775_250	-7.750	0.250

Table 3. Probe weights used in the sensitivity analysis of the averaging procedure (Configuration 1).

k	wk Approach A	wk Approach B
1	1/7	1/4
2	1/7	1/10
3	1/7	1/10
4	1/7	1/10
5	1/7	1/10
6	1/7	1/10
7	1/7	1/4

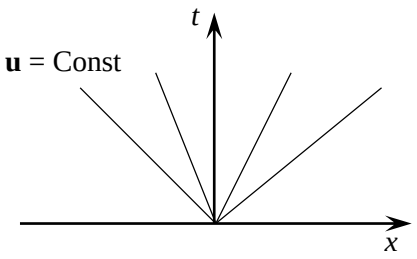

Figure 1. Self-similarity of the flow solution in the (x, t) space. The lines u = Const are straight lines.

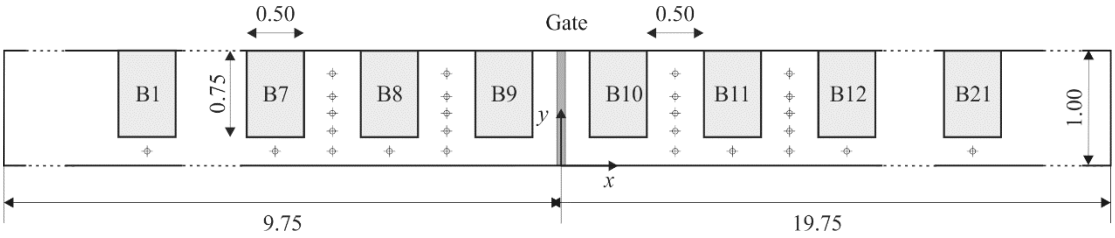

Figure 2. Definition sketch and dimensions (m) for Configuration 1

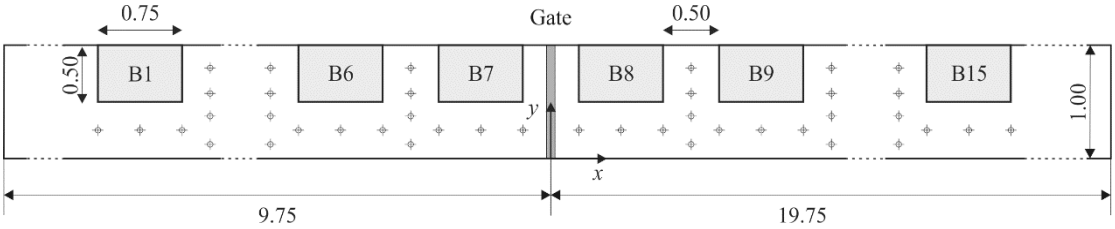

Figure 3. Definition sketch and dimensions (m) for Configuration 2

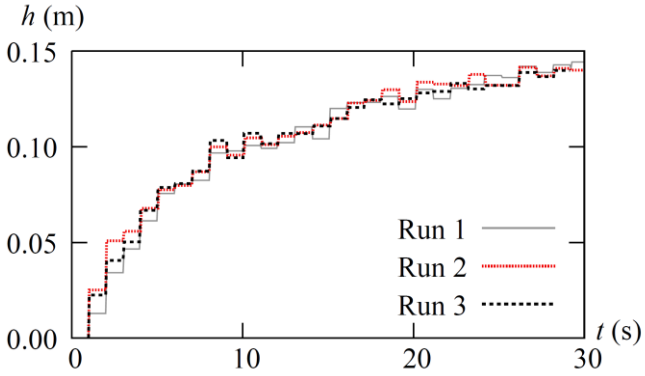

Figure 4. Repeatability of the experiment for Configuration 1, probe PD2_125

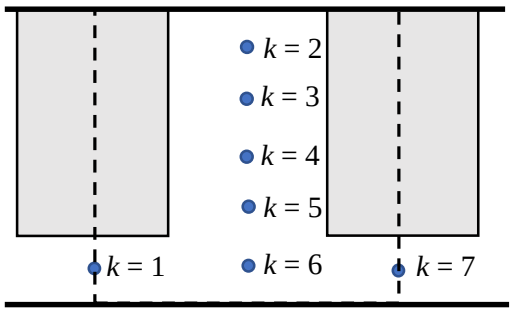

Figure 5. Configuration 1. Probe numbering within a block period. Dashed lines: boundaries of the block period.

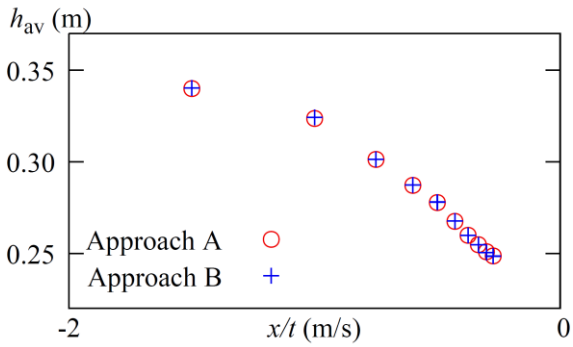

Figure 6. Sensitivity analysis of the averaging approach. h_{av} computed using Approaches A and B (Configuration 1).

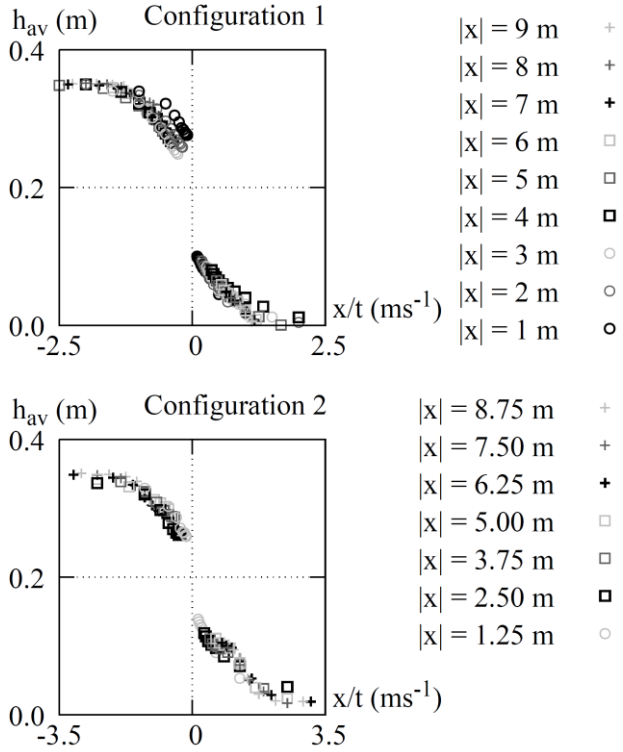

Figure 7. Block-averaged water depth as a function of x/t.

554

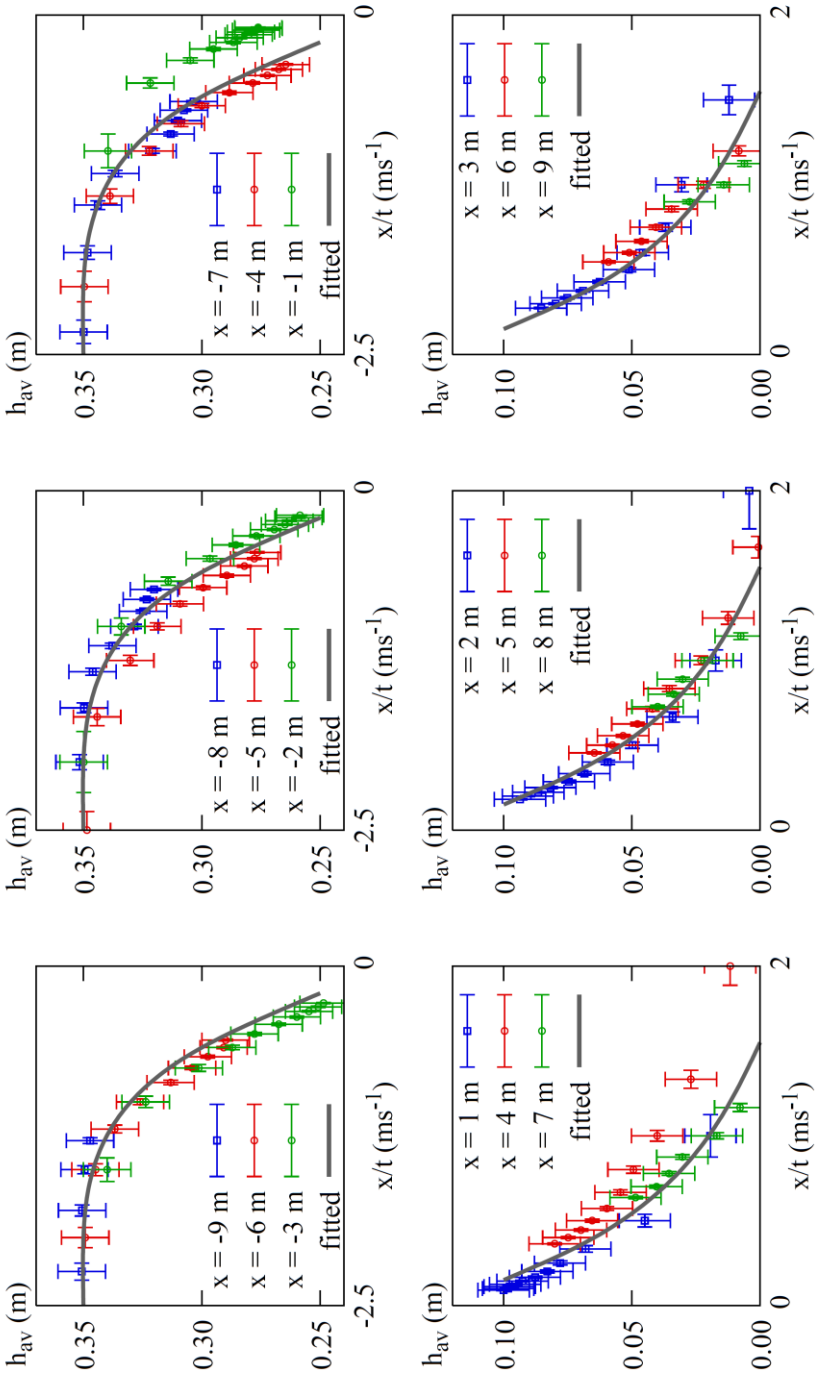

555
556 **Figure 8. Configuration 1. Experimental uncertainty and fitted curve for solution self-similarity**
557 **assessment.**
558

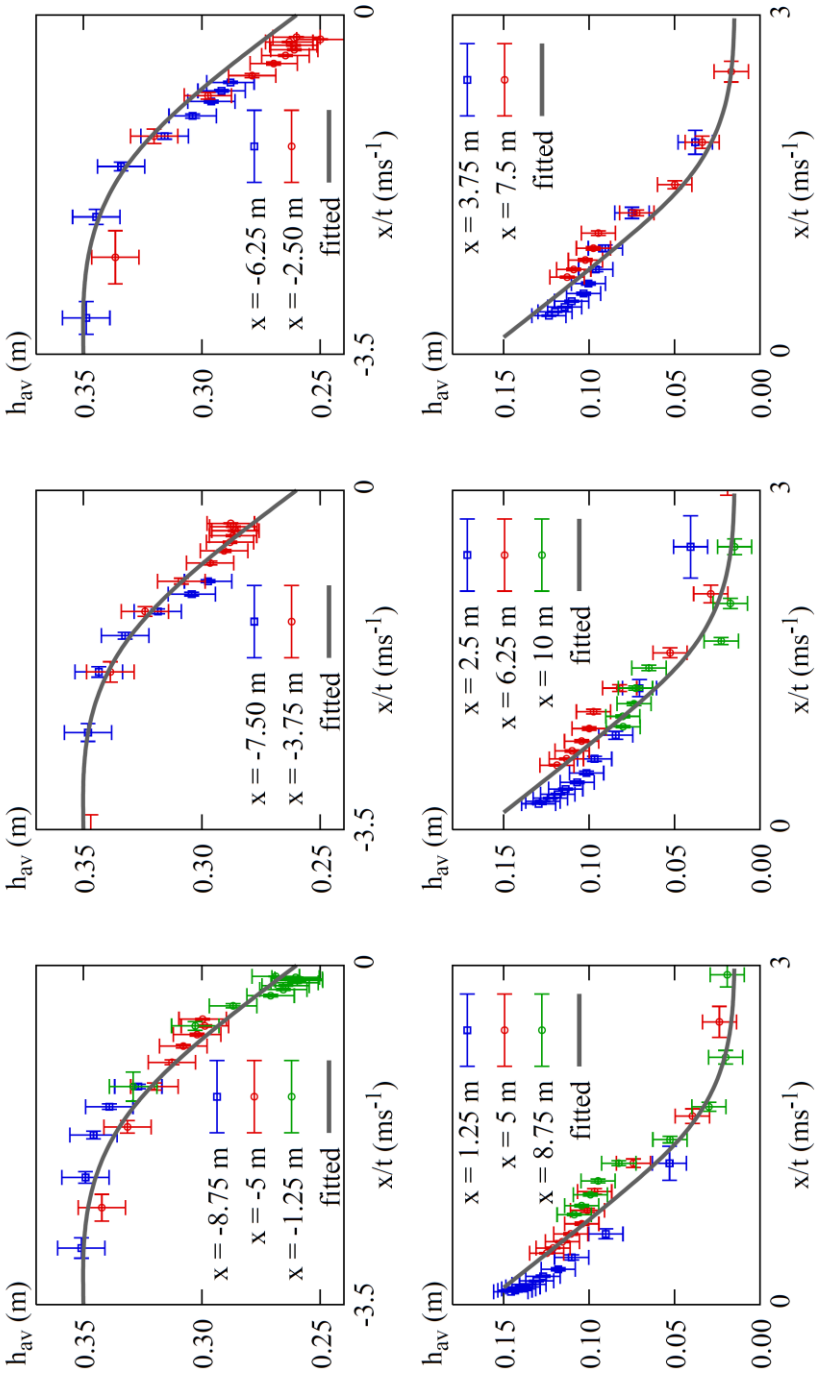

Figure 9. Configuration 2. Experimental uncertainty and fitted curve for solution self-similarity assessment.

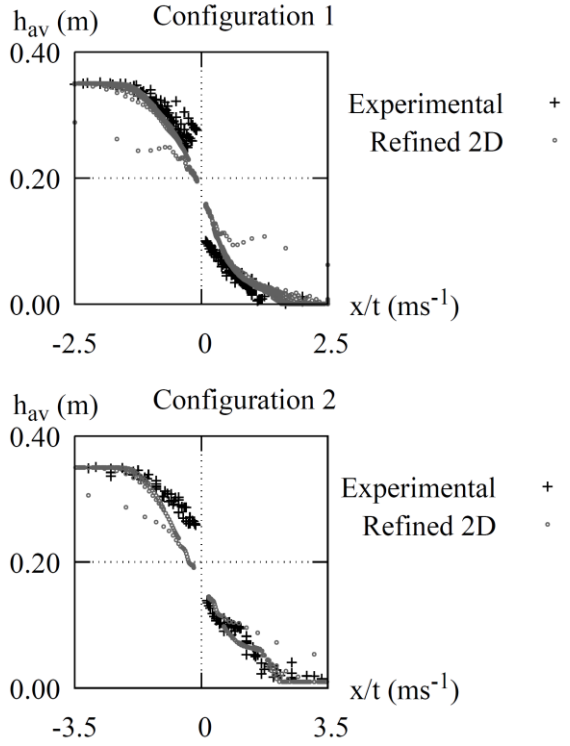

Figure 10. Comparison of the block-averaged refined 2D shallow water solution and experimental results.

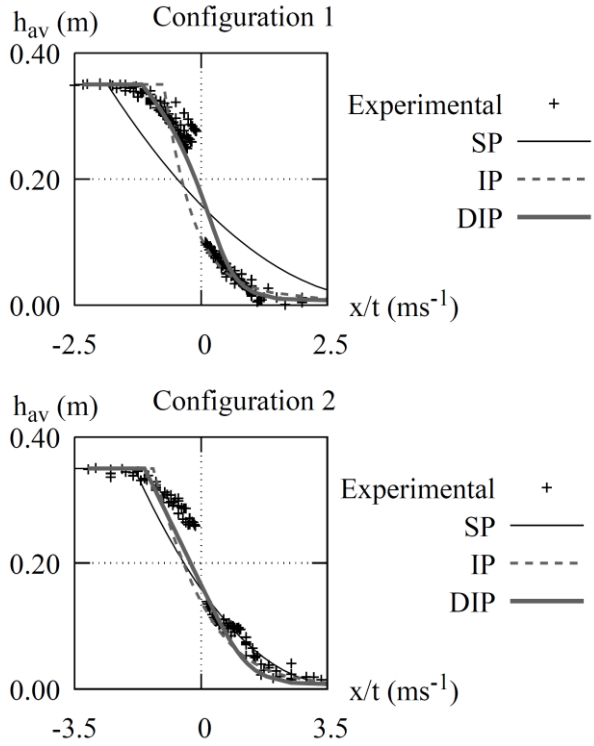

Figure 11. Comparison of the SP, IP and DIP porosity model solutions and experimental results.